Photofragment Spectroscopy and Predissociation Dynamics of Weakly Bound Molecules

Hanna Reisler

Department of Chemistry, University of Southern California, Los Angeles, California 90089-0482; email: reisler@usc.edu

Annu. Rev. Phys. Chem. 2009. 60:39–59

First published online as a Review in Advance on October 13, 2008

The *Annual Review of Physical Chemistry* is online at physchem.annualreviews.org

This article's doi: 10.1146/annurev.physchem.040808.090441

0066-426X/09/0505-0039$20.00

Key Words

dimers, hydrogen-bonded complexes, imaging, photoelectrons, photoions

Abstract

Photofragment spectroscopy is combined with imaging techniques and time-resolved measurements of photoions and photoelectrons to explore the predissociation dynamics of weakly bound molecules. Recent experimental advances include measurements of pair-correlated distributions, in which energy disposal in one cofragment is correlated with a state-selected level of the other fragment, and femtosecond pump-probe experiments, in some cases with coincidence detection. An application in which coincident measurements are carried out in the molecular frame is also described. To illustrate these state-selective and time-resolved techniques, we review two recent applications: (*a*) the photoinitiated dissociation of the covalently bound NO dimer on the ground and excited electronic states and the role of state couplings and (*b*) the state-selected vibrational predissociation of hydrogen-bonded acetylene dimers with HCl (acid) and ammonia (base) and the importance of angular momentum constraints. We highlight the crucial role of theoretical models in interpreting results.

1. INTRODUCTION

Photofragment spectroscopy: spectroscopy in which a specific property (e.g., wavelength, velocity, angle, or time) is varied while monitoring a state-selected photofragment

VMI: velocity map imaging

Vibrational predissociation (VP): indirect dissociation process from a bound state excited to above its dissociation limit

For over a quarter of a century, photofragment spectroscopy has served as an important and multifaceted experimental tool for studies of photoinitiated reactions in molecular beams because it is often easier to monitor a reaction product than the parent species. Initially, state-selected photofragments were monitored as a function of laser excitation wavelength, but later the technique was broadened to encompass a large variety of properties. For example, photofragments include atoms, molecules, and electrons. Monitored properties include the molecule's excitation wavelength to obtain partial cross sections for the production of state-selected fragments, the fragment detection wavelength to obtain its internal states, the translational energy of a state-selected fragment to derive the correlated internal states of the cofragment, the ejection angle to determine the symmetry of the electronic transition, and the time evolution to study kinetics and identify couplings among electronic states. As experimental techniques have evolved, photofragment spectroscopy has expanded its scope, resolution, sophistication, and the types of photoinitiated processes it can probe (1–5).

An advantage of photofragment spectroscopies is that they allow the examination of a scientific issue from multiple perspectives, affording complementary views that can be integrated to generate a comprehensive picture. The results also provide benchmarks for theories and can help generate new theoretical models to be tested with different state-specific data sets.

Most important, photofragment spectroscopy is a means to an end. It is applied in answering a specific scientific question; hence its scope and capabilities are best illustrated by example. In this review, I use this broad definition of photofragment spectroscopy and focus on applications involving photoelectron and photoion velocity map imaging (VMI) (1–5) of weakly bound molecules. The ability to switch rapidly between photoions and photoelectron detection (or even to monitor them in coincidence) is a major advantage of the imaging technique. The scientific emphasis is on the vibrational predissociation (VP) of weakly bound molecules (covalently or hydrogen bonded) that are too complex to elucidate by experiment or theory alone, and the dynamics perspective is highlighted throughout. This review does not attempt to be exhaustive; rather, it focuses on specific systems that illustrate general issues and capabilities. I hope to show that with the experimental methods now available and advances in high-level theory, significant progress can be achieved in understanding the dynamics of complex systems that were beyond reach even a few years ago.

I first summarize briefly the experimental techniques and then describe the VP dynamics of three weakly bound systems: the covalently bound NO dimer and hydrogen-bonded dimers of acetylene with HCl and ammonia. In the NO dimer (or more correctly *cis*-ONNO), the issue is how the chemical nature of the weak covalent N-N bond ($\sim$700 cm^{-1}) influences the predissociation dynamics in the ground electronic state and in electronic states excited in the ultraviolet (UV) region. It was only through the confluence of sophisticated experiments and high-level theory that real progress has been achieved, but several issues remain. The acetylene-dimer studies examine energy flow and VP dynamics in dimers in which the acetylene subunit serves either as a Lewis acid or as a base.

2. EXPERIMENTAL TECHNIQUES

Although there are many different techniques to study VP, most work described here exploits photoion and photoelectron imaging. This popular and versatile technique (1–7), in particular its VMI variant (6), now routinely achieves a resolution of $\Delta E/E \sim 2\%$ or better. Most of its features have been described in a book (1) and a recent review (7) and are not elaborated on further here.

Briefly, in VMI (6) a state-selected product is ionized by a polarized laser photon, and the extracted ion cloud expands while traveling in a field-free region toward a position-sensitive detector. By reversing the extraction voltage polarity, one can detect photoelectrons as well. In VMI, the electrostatic lens system is optimized such that ions of the same velocity reach the same position on the detector, regardless of their positions in the overlap region of the dissociation (pump) and detection/ionization (probe) lasers (6–9). The expanded charged-particle cloud creates a two-dimensional (2D) projection on the detector that contains all the essential information on the velocity distribution of the selected product. In the work described herein, the images possess cylindrical symmetry around the polarization vector of the dissociation laser, which lies parallel to the detector plane. It is then possible to invert the 2D image to a 3D velocity distribution, and any cut through the center graphically displays the velocity (momentum) of the particle (which is proportional to the distance from the center of the image) and its angular distribution (1). The angular distribution of the product is described for one-photon excitation by the formula

$$I(\theta) = c\,[1 + \beta P_2(\cos\theta)],$$

where θ is the angle between the charged-particle velocity vector and the laser polarization direction, $I(\theta)$ is the intensity at angle θ, $P_2(\cos\theta)$ is the second Legendre polynomial, β is the recoil anisotropy parameter, and c is a constant. In multiphoton processes, higher-order $\beta_n P_n(\cos\theta)$ terms must be included, and for the polarization conditions employed here, n is even (1, 2). The charged-particle detector is coupled to a phosphor screen, and the emitted light is detected by a CCD (charge-coupled device) camera. Several methods of image reconstruction exist (1), and in our work we use the BASEX (basis set expansion) method (10).

The imaging arrangement can be used to probe other properties of the dissociation in addition to velocity (or kinetic-energy release) and angular distributions. These include the following: (*a*) photofragment spectroscopy, achieved by monitoring the total charged-particle signal reaching the detector as a function of excitation wavelength (1, 2); (*b*) time-resolved (TR) photoion or photoelectron spectroscopy, in which the time evolution of a product is mapped by varying the delay between the pump and probe lasers, usually in the 100–3000-fs range typical of many dissociation processes and nonadiabatic transitions between electronic states (3, 4); and (*c*) time-resolved coincidence imaging spectroscopy (TRCIS), which affords coincident detection of two selected products and unravels additional correlations and their time evolution (see Section 3.4) (11, 12).

Photoelectrons: electrons ejected by photon absorption from the ground or excited electronic state

TR: time-resolved

TRCIS: time-resolved coincidence imaging spectroscopy

CT: charge transfer

3. NO DIMER OR *CIS*-ONNO? THE INTRIGUING CASE OF GAS-PHASE N_2O_2

3.1. Electronic Structure and Covalent Bonding

The nitric-oxide dimer $(NO)_2$ has attracted much experimental and theoretical attention because of the nature of its weak covalent N-N bond and the complexity of its photodissociation dynamics. The equilibrium geometry of gas-phase $(NO)_2$ is trapezoidal *cis*-planar (13, 14) (**Figure 1**), and the dimer is weakly (although covalently) bound by 708 ± 10 cm^{-1} (15–17).

The N-N bond is so weak because it results from the coupling of two electrons in antibonding π^* orbitals of the monomers (**Figure 1**). Crucial to understanding the electronic structure is recognizing that there are several nearly degenerate ways to orient the π^* orbitals and hence several possibilities of arranging the two unpaired electrons. These arrangements can result in diradical-like configurations in which the electron density is shared equally between the two monomers or ion-pair charge-transfer (CT) arrangements (18–24). Interactions among these π^*

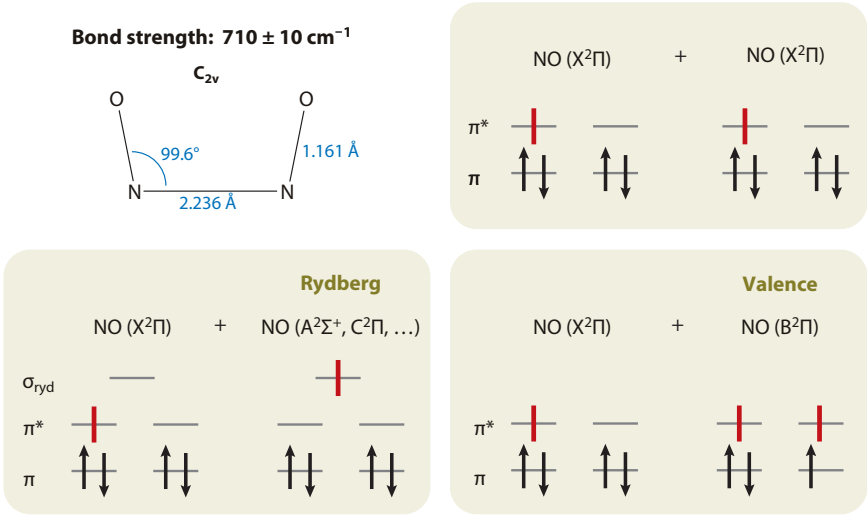

Figure 1

(*Upper left*) The geometry of the NO dimer. The two unpaired electrons of the NO monomers that lead to specific product channels are shown schematically in red for several product-state combinations.

orbitals give rise to four orbitals: Two are in plane [$\sigma(a_1)$ and $\sigma^*(b_2)$] and two are out of plane [$\pi(b_1)$ and $\pi^*(a_2)$]. The lowest electronic states arise from distributing two electrons among nearly degenerate orbitals, which results in a large number of low-lying electronic states (e.g., eight states are clustered within 1 eV of the ground state, and the rest are at energies >5 eV) (19, 22, 23). Several of the higher states have CT configurations that are bound diabatically with respect to $NO^+ + NO^-$. The lowest-lying group of states correlates with two NO fragments in the ground electronic state $X^2\Pi$, which except for the bound ground state are all repulsive (**Figure 2**) (19–23):

$$cis\text{-}ONNO(^1A_1) \rightarrow NO(X^2\Pi) + NO(X^2\Pi) \quad \Delta H = 708\ cm^{-1}(0.088\ eV). \tag{1}$$

This electronic complexity requires advanced electronic structure treatment that is still a challenge for theory (19–24).

Even more challenging are the electronic states excited in the 240–180-nm UV region (18, 19, 22, 23), in which both valence and Rydberg states lie. This strong ($f = 0.36$) dimer absorption (18, 25, 26) can be detected readily just to the red of the absorption of the NO monomer in a seeded molecular beam with a few percent NO.

Experiments show that the state reached in this region is a valence state of B_2 symmetry (18, 27), and two product channels in which one fragment is either in the Rydberg $NO(A^2\Sigma^+;3s)$ or in the valence $NO(B^2\Pi)$ state are dominant (**Figures 1** and **2**) (27–29):

$$cis\text{-}ONNO(^1A_1) \rightarrow NO(X^2\Pi) + NO(A^2\Sigma^+) \quad \Delta H = 44{,}910\ cm^{-1}(5.57\ eV) \tag{2}$$

$$\rightarrow NO(X^2\Pi) + NO(B^2\Pi) \quad \Delta H = 46{,}248\ cm^{-1}(5.73\ eV). \tag{3}$$

Most relevant to experiments are Levchenko et al.'s (22) recent high-level electronic structure calculations, which illustrate the extraordinary difficulties in calculations when several valence and Rydberg states overlap. Their striking finding is the existence of a very bright diabatic CT (valence) state of B_2 symmetry that carries the transition oscillator strength and is mixed with a large number of Rydberg and valence states (22, 30).

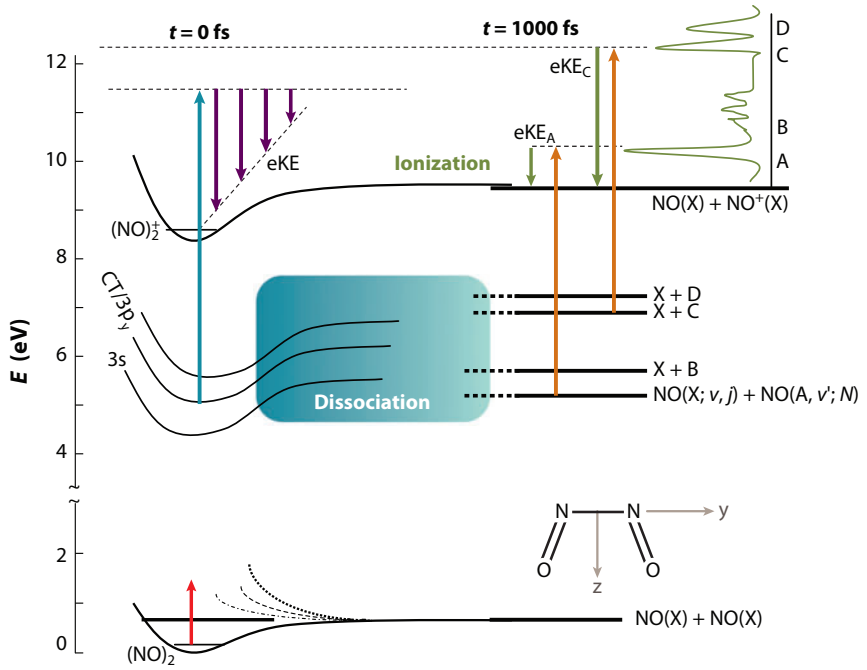

Figure 2

Schematic diagram of dissociation and ionization processes in the NO dimer. At the bottom, the vibrational predissociation of the ground electronic state of the dimer is shown (*red arrow*), as well as the existence of low-lying repulsive states. The blue arrow above depicts ionization from the excited charge-transfer (CT)/$3p_y$ electronic states, and the purple arrows going down display the broad range of energies of the ejected photoelectrons. The orange arrows on the right display the photoionization of NO(A) and NO(C) products, and the green arrows depict the expected energies of the corresponding photoelectrons ejected from these Rydberg states. The spectrum on the far right shows schematically the photoelectron kinetic energies (KE) expected from photoionization of NO products in the A, B, C, and D states. The blue box refers to the complex evolution of the excited CT/$3p_y$ state toward products. The coordinate axis system used to label the electronic states is also shown.

These calculations show that the lowest adiabatic states that have CT contributions are admixtures with the B_2 Rydberg $3p_y$ state, along the N-N bond (**Figure 2**), and the extent of the $3p_y$ character depends on the N-O distance. The B_2 ($3p_y$) Rydberg state correlates with the out-of-phase combination of $NO(X^2\Pi) + NO(A^2\Sigma^+;3s)$ wave functions, whereas the equivalent in-phase combination yields the $A_1(3s)$ Rydberg state of the NO dimer, which lies at lower energy (**Figure 2**). Thus, both the 3s and $3p_y$ Rydberg states correlate with channel 2 (see below).

Levchenko et al. used an exciton-like physical picture to explain the complex electronic structure of $(NO)_2$. Their calculations (22) show that (*a*) numerous electronic states in the 5–9-eV region have CT and Rydberg character; (*b*) a single B_2 CT state lends brightness to states at ~5–7 eV, resulting in several adiabatic states of mixed CT/Rydberg character; and (*c*) when the molecule absorbs a UV photon, it enters the diabatic CT state that has a bound $-1/R$ attractive potential, and in order to dissociate it must evolve into adjacent Rydberg or valence states. Finally, they conclude that at present no single theoretical method can account for all the states; therefore, there is still some uncertainty regarding excitation energies, the state composition, and the variation of electronic configuration with geometry change.

3.2. Vibrational Predissociation on the Ground Electronic State: Seeking Signatures of Excited Electronic States

Intramolecular vibrational redistribution (IVR): coupling among molecular vibrational levels that have similar energies

The goal of these experiments was to determine energy disposal and assess the role of the repulsive low-lying electronic states (<1 eV) (19–21). Because of the disparity between the strength of the N-O and N-N bonds, dissociation following excitation of N-O stretch vibrations displays evidence of restricted intramolecular vibrational redistribution (IVR) (15, 16, 31–36) often associated with the VP of weakly bound species.

In an elegant series of experiments, Casassa and colleagues (15, 32–34) first examined VP following N-O stretch excitation in the ground electronic state. They found different lifetimes for ν_1 symmetric (1868 cm^{-1}) and ν_5 asymmetric (1789 cm^{-1}) N-O stretch fundamentals: 880 ± 260 ps and 39 ± 8 ps, respectively (34). In the first overtone region, the lifetimes of the $\nu_1 + \nu_5$ and $2\nu_5$ states were 34 ± 6 ps and 20 ± 3 ps, respectively (15), and one of the NO($X^2\Pi$) products was preferentially in $v = 1$. These results indicate that the NO asymmetric stretch is more efficiently coupled to the N-N dissociation coordinate. Only 3%–12% of the energy was deposited in product rotation, whereas the percent of energy in translation was several times higher. Dissociation fragments appeared mostly as $NO(X^2\Pi_{1/2}) + NO(X^2\Pi_{3/2})$ pairs, and internal energy distributions were nonstatistical. Two mechanisms have been considered in explaining the energy disposal: electronically nonadiabatic VP and vibrational potential coupling that takes place solely on the ground-state surface (15, 34). Additionally, a hybrid mechanism has been proposed in which the total dissociation rate is determined predominantly by nonadiabatic crossings, whereas partial rates to specific product channels are affected by further vibrational potential couplings (35, 36).

Coupling to repulsive electronic states in the Franck-Condon region could be state specific; therefore, Potter et al. (37) extended these measurements to higher NO-stretch overtones and combination bands at 3600–7500 cm^{-1}, at which vertical excitation to low-lying electronic states is expected. However, no state-specific couplings were found upon excitation in the $3\nu_5$, $2\nu_1 + \nu_5$, $\nu_1 + 3\nu_5$, and $3\nu_1 + \nu_5$ bands, and NO rotational and spin-orbit distributions were qualitatively similar to those observed at lower excitation energies.

Distinct patterns, however, have emerged in the vibrational excitation of NO. VP occurs primarily via $\Delta v = -1$ processes, as is typical of van der Waals complexes, yet vibrational energy resides mainly in one of the two NO fragments. This may reflect an increased local-mode character of NO-stretch overtone wave functions that project onto products. $\Delta v = -2$ processes are more prevalent in the predissociation of levels with a large number of quanta in the asymmetric NO-stretch mode ν_5, which are more strongly coupled to the N-N dissociation coordinate (37).

Potter et al. (37) proposed that vibrational nonadiabatic coupling following the loss of a vibrational quantum takes place at shorter N-N separations than spin-orbit couplings, which are determined at a longer range in which several potential curves coalesce (**Figure 2**). The modest fragment rotational excitation is likely related to the geometry of the complex, the shallowness of the well, and the anisotropy of the potential. There was no evidence of direct excitation to higher electronic states.

3.3. Ultraviolet Photodissociation from Coupled Valence/Rydberg States

To date, most UV photodissociation experiments within the strong $B_2 \leftarrow A_1$ system ($f = 0.36$, peak at 205 nm) (18, 25, 26) have examined dissociation to channels 2 and 3 (16, 27–31, 38–43). Identifying the absorbing states and their evolution to products turned out to be quite a challenge, with some results still contradictory. Because the absorption spectrum is broad and largely featureless (18, 25, 26, 41), it is difficult to determine how many electronic states are accessed at 193–242 nm. Most experimental evidence came from photoelectron spectroscopy

studies in which an electron was ejected from the excited electronic state either with a nanosecond or femtosecond laser.

3.3.1. Photoelectron spectroscopy: identifying the absorbing state and its time evolution. As described above, ab initio calculations show that the oscillator strength in the UV region is carried by a very bright CT valence state of B_2 symmetry, which is diabatically bound and correlated with NO^+ and NO^- products (19, 22). This state is mixed with (or lends oscillator strength to) a large number of adiabatic states that correlate asymptotically with fragments in which one of the NOs is in an excited Rydberg or valence state (**Figure 2**). The lowest adiabatic B_2 state correlates with channel 2. At higher energies, the asymptote of channel 3 is reached, and those of the Rydberg $NO(C^2\Pi)$ and $NO(D^2\Sigma^+)$ fragments (at 6.58 and 6.7 eV, respectively; see **Figure 2**) are reached at even higher energies. For example, Naitoh et al. (28, 29) observed fluorescence from NO in both Rydberg (A) and valence (B) states at 193 nm, whereas Dribinski et al. (44) identified NO in Rydberg (A, C, and D) and valence (B) states in two-photon excitation experiments at 160–180 nm by photoelectron imaging of these products.

At longer wavelengths (just above and below the channel 2 threshold at $\lambda \leq 222.67$ nm), the bright state is the lowest of the two mixed B_2 CT/$3p_y$ states (**Figure 2**). By using nanosecond lasers at wavelengths below this threshold, Dribinski et al. (30) detected both photoions and photoelectrons by ionizing from this state (**Figure 3*a*,*b***). They placed its origin ~3600 cm^{-1} below channel 2, i.e., at 41,300 cm^{-1} (5.12 eV), in good agreement with theory (22). At higher energies, the second CT/$3p_y$ adiabatic state (calculated to lie ~0.4 eV above) can also be reached. The transition to the $A_1(3s)$ state (~0.5 eV below the lowest B_2 state) is weak (22).

In nanosecond laser experiments, once channel 2 opens, it is impossible to detect any longer the parent photoelectron spectrum, and only photoelectrons ejected from the product $NO(A^2\Sigma^+)$ Rydberg state are observed (**Figure 3*c***), implying that dissociation to channel 2 competes effectively with ionization. In contrast, no abrupt change in excited-state lifetime is observed in the TR femtosecond measurements (39, 41), with lifetimes decreasing gradually from ~1 ps to ~200 fs as the wavelength decreases from 232 to 200 nm. However, nanosecond and femtosecond lasers do not create the same initial wave packet of excited states, and one needs to exercise caution when comparing results from these two experiments. In femtosecond laser experiments, it is still possible to observe ionization of the parent at early times even at short wavelengths, whereas at later times NO(A) ionization dominates (**Figure 3*d***) (38–42).

What is common to all excitation wavelengths is that the photoelectron spectra are broad, structureless, and dominated by slow electrons (30, 38–42), indicating that photoionization takes place from a valence, rather than a Rydberg, state. How the bright state dephases and photoionizes is still somewhat of a mystery. Theoretical calculations show that neither the CT state nor the Rydberg states differ much in their equilibrium geometries from the ion ground state (22, 42). Thus, in ionizing the CT state, one expects a fairly sharp photoelectron spectrum with short progressions and a dimer ion with only a modest amount of internal energy. In contrast, most generated ions have internal energies that exceed the dissociation threshold, even when reached via excitation near the origin of the lowest B_2 state, and the main 1 + 1 photoionization product is NO^+ rather than $(NO)_2^+$ (30, 41, 42). Obviously, the initial wave packet dephases quickly, and the range of geometries sampled by photoionization is extended. Several photoionization scenarios have been put forth that involve the time evolution of the excited state along the N-N and N-O coordinates (22, 41, 42), but no definitive description exists at this time.

Analyses of the TR photoelectron spectra results have been the subject of some controversy. In their first paper, Blanchet & Stolow (38) reported TR photoelectron spectra following 210-nm excitation, which they analyzed using two timescales. Suzuki and coworkers (39–41), conversely,

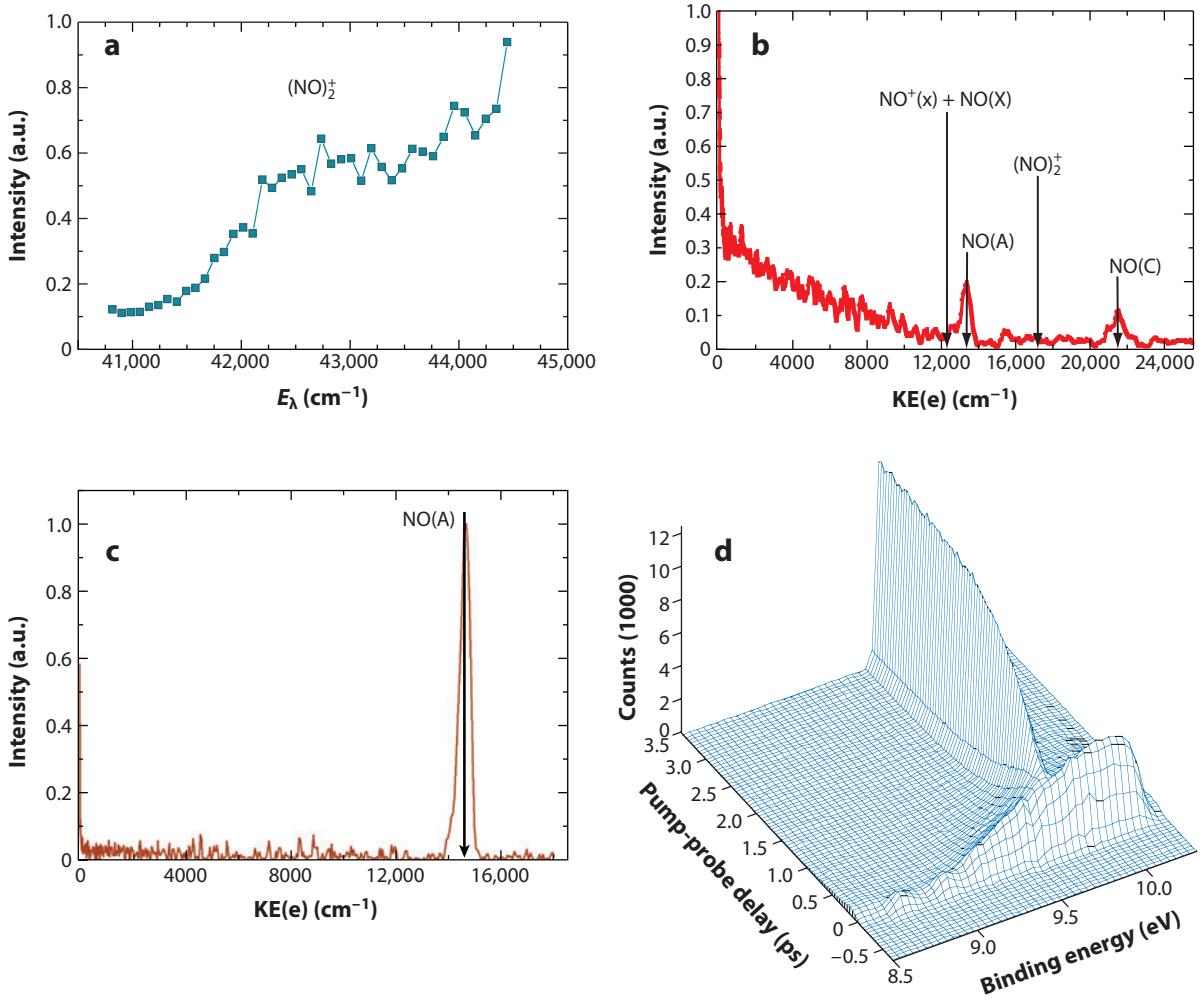

Figure 3

(*a*) Photofragment yield spectrum of $(NO)_2^+$ ions obtained by photoionization of the excited charge-transfer (CT)/$3p_y$ electronic state of the NO dimer by using nanosecond 1 + 1 photon ionization at the indicated excitation energies. The origin of absorption is placed at ~41,300 cm^{-1}. (*b*) Photoelectron kinetic-energy (KE) distribution obtained by nanosecond 1 + 1 ionization at 228 nm. The black arrows indicate the energetic thresholds for the formation of the dimer parent ion and fragment NO^+ from dissociative photoionization. The peaks marked NO(A) and NO(C) derive from higher-order processes (30). (*c*) Photoelectron KE distribution obtained following nanosecond laser excitation of the NO dimer at 221.67 nm, above the opening of the NO(X) + NO(A) channel. The narrow peak corresponds to one-photon ionization of the NO(A) product (30). (*d*) Time-resolved femtosecond photoelectron spectrum obtained by excitation at 209 nm and ionization at 279.5 nm (42). The binding energy of the photoelectron is shown on one axis, and another axis depicts the pump-probe time delay in picoseconds. The vertical axis shows the intensity of the photoelectron signal. Early times depict photoionization of the dimer ion as in panel *b*, whereas at later times, the narrow peak from the ionization of NO(A) products dominates, as in panel *c*. Figure adapted from data in References 30 and 42.

fit their TR traces (obtained at similar wavelengths) with one decay time constant and reported an additional small feature, which they interpreted as a signature of the 3s dimer state. Stolow and coworkers (42) later repeated their measurements with better sensitivity and resolution and still had to use two time constants, although their new lifetimes were somewhat different than first reported. They saw no evidence of coupling to the 3s state. Their interpretation, supported by

recent theoretical calculations, is that with 200–210-nm excitation, the initial state accessed after dephasing of the bright CT state is the second adiabatic CT/3p_y state, which evolves to products via the 3p_y state (22). Their most recent results, obtained by TRCIS (42), also indicate evolution of the CT state to the 3p_y state before dissociation (see below).

3.3.2. Imaging exit-channel dynamics to NO($X^2\Pi$) + NO($A^2\Sigma$; 3s). We now turn our attention to energy distributions in the NO($X^2\Pi$) + NO($A^2\Sigma$;3s) products following excitation to the CT/3p_y state(s) and assess whether the excited NO dimer behaves similar to a van der Waals complex or the dynamics is dominated by the covalent nature of the N-N bond in the bound excited state. Here we exploit two important observables of VMI: pair-correlated product-state distributions derived from translational energy measurements of state-selected fragments and angular distributions measured as a function of fragment recoil energy.

Naitoh et al. (27) first determined state distributions and some vector correlations in NO(A) products at 193 nm, concluding that the excited state was repulsive, even though product-state distributions were well described by a constrained version of statistical phase-space theory. In their version, they treated the fraction of products with an aligned orbital angular momentum (AM) vector as a parameter that depended on the rotational energy of the NO products. The NO product exhibited weak alignment, and the vector correlations indicated a preference for planar dissociation. The recoil anisotropy parameter, β_{eff}, ranged from 1.0 to 1.4 for N = 7–20 levels of NO(A) (where N is the rotational level), typical of parallel transitions. These results, which correspond to excess energy $E^\dagger = 6900\ cm^{-1}$, were interpreted as an indication of fast and direct dissociation from a state of B_2 symmetry (27).

Using VMI of selected NO(A, N) levels, Demyanenko et al. (31) and Potter et al. (16) obtained pair-correlated center-of-mass recoil energies and speed-dependent values of β_{eff} at lower excess energies, $E^\dagger = 200$–$2038\ cm^{-1}$. For $E^\dagger = 2038\ cm^{-1}$, they found that both the rotational energy distribution of NO(X) cofragments (**Figure 4**) and the global rotational state distribution of NO(A) deviated from the predictions of phase-space theory, but the deviations were rather small. They proposed that effects due to exit-channel dynamics influenced the rotational state distributions. The average values of β_{eff} decreased with decreasing excess energy, indicating an increase in dissociation lifetime, in agreement with direct TR measurements (16, 39).

For each NO(A, N) image, as the fragment translational energy E_T decreased, β_{eff} first decreased from its limiting value at high E_T and then increased abruptly again at very low E_T (**Figure 4*b***) (16, 31). This β-E_T correlation could be well simulated with a classical model (31, 45, 46) that related the decrease in β_{eff} to deviations from axial recoil at low E_T mandated by AM conservation. The simulations show also that high rotational states J of the NO(X) cofragment are produced preferentially via planar dissociation, and the fragments' angular momenta become fixed at an interfragment separation of ~2.6 Å, close to the 2.24-Å N-N equilibrium bond length in the ground state of the dimer. Potter et al. (16) compared their pair-correlated results with vector and scalar properties predicted by statistical theories (47) and concluded that the propensity for planarity (i.e., velocity $\boldsymbol{v}$ perpendicular to J for high J's) does not agree with a statistical behavior and must originate in exit-channel dynamics.

Vibrational excitation in the fragments increases as the excitation energy increases (16, 31, 41, 44). However, the vibrational levels are distributed nonstatistically in the two fragments, with one fragment receiving more vibrational excitation, similar to dissociation via channel 1 (37). When one fragment is in a Rydberg state (such as A, C, or D), this fragment is colder than NO(X), which is born with high vibrational excitation (44). Thus, whereas vibrational energy is high and center-of-mass translation is low (as is typical in weakly bound complexes), the projections of the excited parent wave functions onto fragment vibrational levels exhibit state-specific effects.

Phase-space theory: a statistical theory that apportions products' quantum states democratically, satisfying energy and angular momentum conservation

AM: angular momentum

β-E_T model: describes changes in recoil anisotropy in dissociation due to deviations from axial recoil mandated by conservation of angular momentum

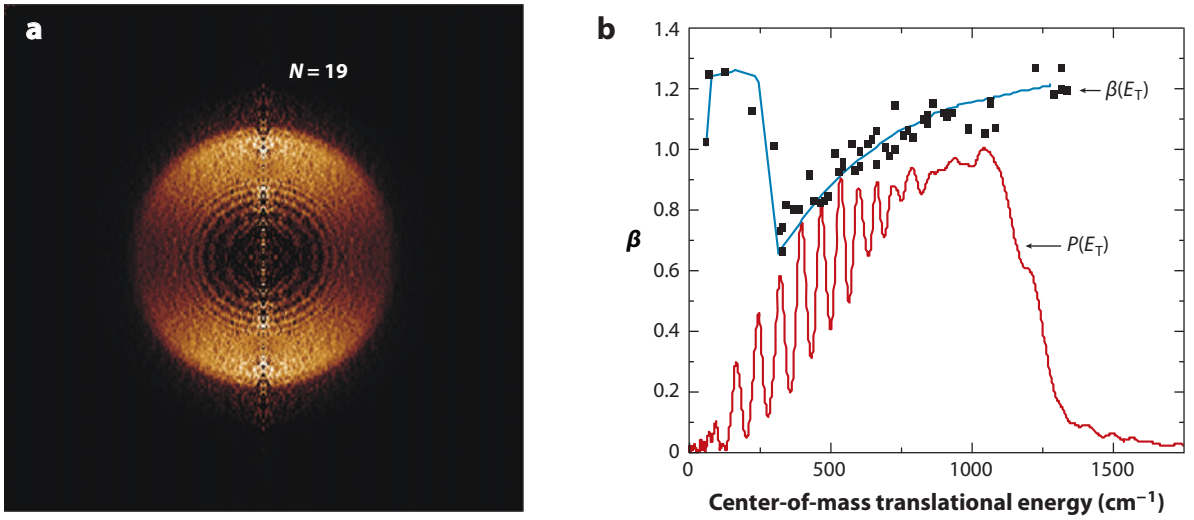

Figure 4

(*a*) An image obtained by monitoring the NO(A, $N = 19$) product of the 213-nm photodissociation of the NO dimer by using 1 + 1 photon ionization. (*b*) The red curve shows the center-of-mass recoil energy distribution $P(E_T)$ of the fragments. The peaks in the spectra are high rotational levels of the NO(X) cofragment corresponding to the resolved inner rings in the image in panel *a*. The black squares are the recoil anisotropy parameters, β_{eff}, measured at specific recoil energies. The values of β are shown in the vertical axis. The blue curve is the result of the β-E_T model described in Reference 31. Figure adapted from data in Reference 31.

In summary, the energy-disposal studies show that VP in the weakly bound excited state is influenced by exit-channel dynamics and restricted IVR. Specifically, low-frequency torsional (out-of-plane) levels do not couple efficiently to other modes, especially at higher excess energies when the dissociation is fast, thus explaining the propensity for planar dissociation (16, 31). At the same time, long-range attraction between NO(A) and NO(X) encourages IVR and can explain the statistical-like rotational state distributions observed near threshold. Product energy-distribution studies are sensitive to exit-channel interactions but do not shed light on the early time evolution of the excited state.

3.3.3. Time-resolved coincidence photoion and photoelectron imaging. Undoubtedly, the most comprehensive and sophisticated technique brought to bear on NO dimer photodissociation is TRCIS (11, 12). Although to date only a short preliminary report has been published (42), the possibilities are tantalizing. In this method, fully correlated recoil energies and angular distributions of photoelectrons and state-selected photoions are detected in coincidence and measured as a function of time (time resolution ~160 fs). The imaging technique allows not only the determination of angular distributions, but also the analysis of coincident results obtained for selected fragment ejection angles. Moreover, in favorable cases, the technique allows the determination of recoil energy and angular distributions in the molecular frame, rather than in the laboratory frame, which makes it possible to discern features that are masked in laboratory-frame measurements (42). The measured 6D fully correlated sets of data of energy and angular distributions may be cut, projected, and displayed to reveal selected properties and their time evolution. Recent experiments on NO dimer photodissociation are real tours de force. Many data sets have confirmed directly what was only inferred from less correlated results. For example, most photoionization products (obtained in excitation at 209 nm followed by ionization at 279.5 nm) are NO^+ fragments, the

parent $(NO)_2^+$ signals are correlated with fast photoelectrons whose energies correspond to low vibrational excitation in the dimer ion, and the NO^+ ions have high internal energies and correlate with slow photoelectrons.

Because NO^+ from dissociative ionization is ejected predominantly along the direction of the laser polarization axis and the electronic transition dipole moment lies along the N–N bond, the fragment recoil direction peaks around the aligned direction of the N–N bond (molecular-frame *y* axis). In such a case, the recoil frame can coincide with the molecular frame. Geßner et al. (42) selected for analysis only those fragment recoil events in which the NO^+ fragment was directed up or down along the N-N bond (also the pump and probe laser polarization axes). This restriction reduces considerably the averaging in the angular distributions, compared to data observed in the laboratory frame. Indeed, the photoelectron angular distributions obtained in coincidence with the constrained recoil angle of NO^+ at different delay times between the pump and probe lasers show distinct differences as a function of time. Specifically, at a delay of ~330 fs, the fraction of photoelectrons ejected perpendicular to the N-N breaking bond is the largest.

The authors analyzed their photoelectron angular distributions by calculating at each time delay the fraction of partial waves allowed for ionizing a p_y orbital and found that this fraction reaches its maximum at ~330 fs, then subsequently falls. With the aid of recent electron structure calculations (22), they interpreted their results as an indication that the initial CT wave packet evolved to the p_y Rydberg states in less than 300 fs, and then to products with a 590-fs time constant. They saw no evidence for the participation of the 3s Rydberg state of the dimer. However, final scrutiny of these results must await publication of full analysis details.

3.4. Combining Theory and Experiment: What Do We Know So Far?

This section summarizes what is presently known about the predissociation of the NO dimer and what still needs to be resolved. Above I pose a question regarding whether the NO dimer behaves as a covalently bound molecule or a weakly bound complex, and my answer is that it depends. With regard to absorption, *cis*-ONNO provides the correct description, as both calculations and experiments reveal valence absorption bands that have no counterpart in the NO monomer. A more complex picture emerges regarding photodissociation. Although there is a propensity to dispose much of the energy in vibrational excitation of the NO monomers and minimize translational energy release as is common in VP of van der Waals complexes, the distribution of vibrational excitation between the two NO fragments exhibits clear dynamical effects, with one of the NO fragments [NO(X) when the other fragment is NO(Rydberg)] being more highly excited than the other. Rotational energy disposition also deviates from statistical predictions, and vector properties indicate that dissociation is largely constrained to a plane. Thus, the NO dimer behaves similar to a covalently bound species with large disparity between its high-frequency and low-frequency modes that affects IVR, which (combined with exit-channel dynamics) leads to nonstatistical product-state distributions.

Electronic structure calculations have played a crucial role in elucidating the mysteries of the nature of the bright states in UV photodissociation and the propensity to generate NO products in several Rydberg and valence excited states. It is now established that a bright, diabatic CT state is responsible for the strong UV absorption, but because it is deeply bound, it must mix or undergo conical intersections with states whose asymptotes lie above the dissociation thresholds of neutral products. It is the near degeneracy of orbitals with Rydberg, diradical, and ion-pair properties that gives rise to the large number of adiabatic states. The Rydberg formula places the diabatic Rydberg states in the same energy region as the CT states, giving rise to many opportunities for avoided crossings, nonadiabatic couplings, and conical intersections.

It is precisely this multitude of coupling opportunities that makes it so difficult to chart the exact course of evolution from excited parent to products, and despite heroic experimental and theoretical efforts, the picture is still incomplete. Compounding the difficulty is the existence of two mixed CT/Rydberg states within the strong UV absorption band and the fast dephasing of the bright CT state. Thus, whereas only the lowest CT/p_y state can be reached at the onset of the absorption band, both states might absorb at 193–213 nm, at which most of the detailed TR measurements were carried out.

Also unknown are the exact nature of the levels from which photoionization occurs and the role of the NO(X) + NO(X) channel. Clearly, electron ejection from the excited state takes place at geometries that differ considerably from the equilibrium ground states of the neutral and the cation, and the photoelectron spectra do not change qualitatively when the excitation energy increases by ~1 eV. The exact evolution from initial dephasing to ionization is still somewhat puzzling. For example, the rate deduced from femtosecond TR experiments for photoionization does not change abruptly when channel 2 opens, leading the authors to conclude that the partial cross section to this channel is small (39). In contrast, in nanosecond experiments, Dribinski et al. (30) have observed that both the photoelectron and NO^+ signals from photoionization disappear right at the onset of channel 2, and only signals corresponding to NO(A) products can be detected.

Likewise, the nature of the intermediate states participating in photodissociation at 200–213 nm is still the subject of debate, as analyses of transients in the TR measurements carried out in Stolow's and Suzuki's laboratories differ. The former group could fit the transients well only with two time constants (38, 42), whereas the latter employed one time constant, but interpreted a small signal that preceded the distinct photoelectron peak of NO(A;3s) as a signature of crossing to the dimer's A_1(3s) state (39–41). Stolow and coworkers (42) interpreted their analysis of the TRCIS experiments as an indication that the CT state reached at 209 nm evolved to the $3p_y$ state before dissociating, and they did not observe crossing to the 3s state. Levchenko et al. (22) presented several scenarios for the ensuing dissociation that included restricted IVR and/or nonadiabatic transitions, and their electronic structure calculations did not identify crossings to the 3s state. However, identifying all the crossing seams in a dissociating polyatomic molecule is a daunting task (48); therefore, the probability of crossing to the 3s state far in the exit channel cannot be excluded. That multiple surface couplings do take place has been demonstrated at shorter wavelengths (160–180 nm), at which NO fragments in the A, B, C, and D states are produced simultaneously (44).

The most striking signature in the UV dissociation of the NO dimer is the existence of a very bright CT state that serves as the torch that lights up many adiabatic states, which are admixtures of CT, valence, and Rydberg states (22). Such a situation may not be unique to the NO dimer. Other covalently bound dimers may exhibit similar behavior, such as the NO_2 and ClO dimers.

4. PAIR-CORRELATED PREDISSOCIATION DYNAMICS OF HYDROGEN-BONDED DIMERS

This section briefly describes ongoing work using VMI on the predissociation of hydrogen-bonded dimers consisting of polyatomic subunits. Starting in the early 1920s (49–52), and in particular since Pauling's (53) definitive description of the hydrogen bond, there has been continuous interest in understanding the spectroscopy and dynamics of hydrogen-bonded species in diverse environments (54, 55). In the gas phase, emphasis has been placed on studies in the cold environment of supersonic expansions, with most reports focused on spectroscopy, many appearing in this series (56–64).

The attractive forces that hold these dimers together give rise to distinct fingerprints in vibrational energy flow patterns and VP dynamics. For example, in the case of dimers of ethynes with ammonia, the stronger binding relative to van der Waals complexes gives rise to large frequency shifts of the CH-stretch fundamental and overtones, and to broadening of spectral features (65). Energy disposal following VP should reflect the extent of vibrational couplings within each subunit and/or with the other subunit via intermolecular modes. Because of the disparity between the frequencies of the inter- and intramolecular vibrational modes, IVR is often incomplete, giving rise to nonstatistical predissociation (58).

Spectroscopic work on polyatomic dimers has mostly focused on linewidths and frequency shifts, correlating them with predissociation rates. Miller and coworkers were among the first to extend the work to state-to-state VP dynamics (58, 66), using the HF dimer and its dimer with acetylene as benchmark cases (58, 67–70). His work, and that of others, on small dimers was summarized in a 2001 review (58), and the work described herein extends these studies to more complex dimers at higher resolution and to theoretical modeling.

Acetylene can engage in hydrogen bonds with acids such as HCl via its π-bond and strong bases such as ammonia via its weakly acidic hydrogen. Previous work in which acetylene served as the Lewis base in T-shaped dimers with HF, HCl, and OH demonstrated a strong propensity to populate the CC stretch of the acetylene fragment following excitation in the asymmetric (asym-)CH stretch (58, 66–75). This energy flow pattern is apparently encouraged by a near resonance in the acetylene subunit between one quantum of the asym-CH stretch and the CC stretch plus two quanta of bend (71).

Our recent work used VMI to examine pair-correlated product-state distributions in the VP of the dimers of acetylene with HCl (DCl) and with ammonia. These VP processes are inefficient, and when the dimer finally falls apart, it exhibits state-specific effects in both rotational and vibrational excitations. In the absence of accurate potential energy surfaces, understanding the evolution of these slow processes is a challenge.

We can rationalize many of the results with two approximate models. The Ewing model (76, 77) combines the momentum (or energy) gap law with the requirement that the number of quanta transferred in the dissociation must be minimized. This model predicts correctly the predissociation rate of a large number of complexes, and explains why the preferred predissociation pathway involves high vibrational excitation and small translational energy release. The complementary AM model proposed by McCaffery and coworkers (78–80) is based on linear-to-angular momentum interconversion. It has been used extensively to describe inelastic collisions and more recently rotational distributions in VP of weakly bound dimers. By realizing that hard-shaped potentials are required to explain the high fragment rotational levels often generated, it identifies the principal geometries from which dissociation occurs and reproduces well the rotational distributions.

4.1. Predissociation of the T-Shaped HCl (DCl)-Acetylene Dimer

The first VMI study of a T-shaped, hydrogen-bonded dimer was for the acetylene-HCl (DCl) dimer (**Figure 5**) (81, 82). The infrared spectra of the dimer in the asym-CH and HCl stretch regions were reproduced by photofragment spectroscopy of state-selected HCl(j) fragments (**Figure 5*a***) (71, 83). Images of selected HCl(j) and DCl(j) photofragments were then obtained, and an example demonstrating rotational resolution in the acetylene cofragment is shown in **Figure 5*c*,*d***. From the images, the dissociation energy of the dimer was determined [700 $\pm$ 10 cm^{-1} for HCl, in excellent agreement with theory (84)]. The global HCl(j) and DCl(j) rotational distributions were measured as well and showed a large population in high rotational states.

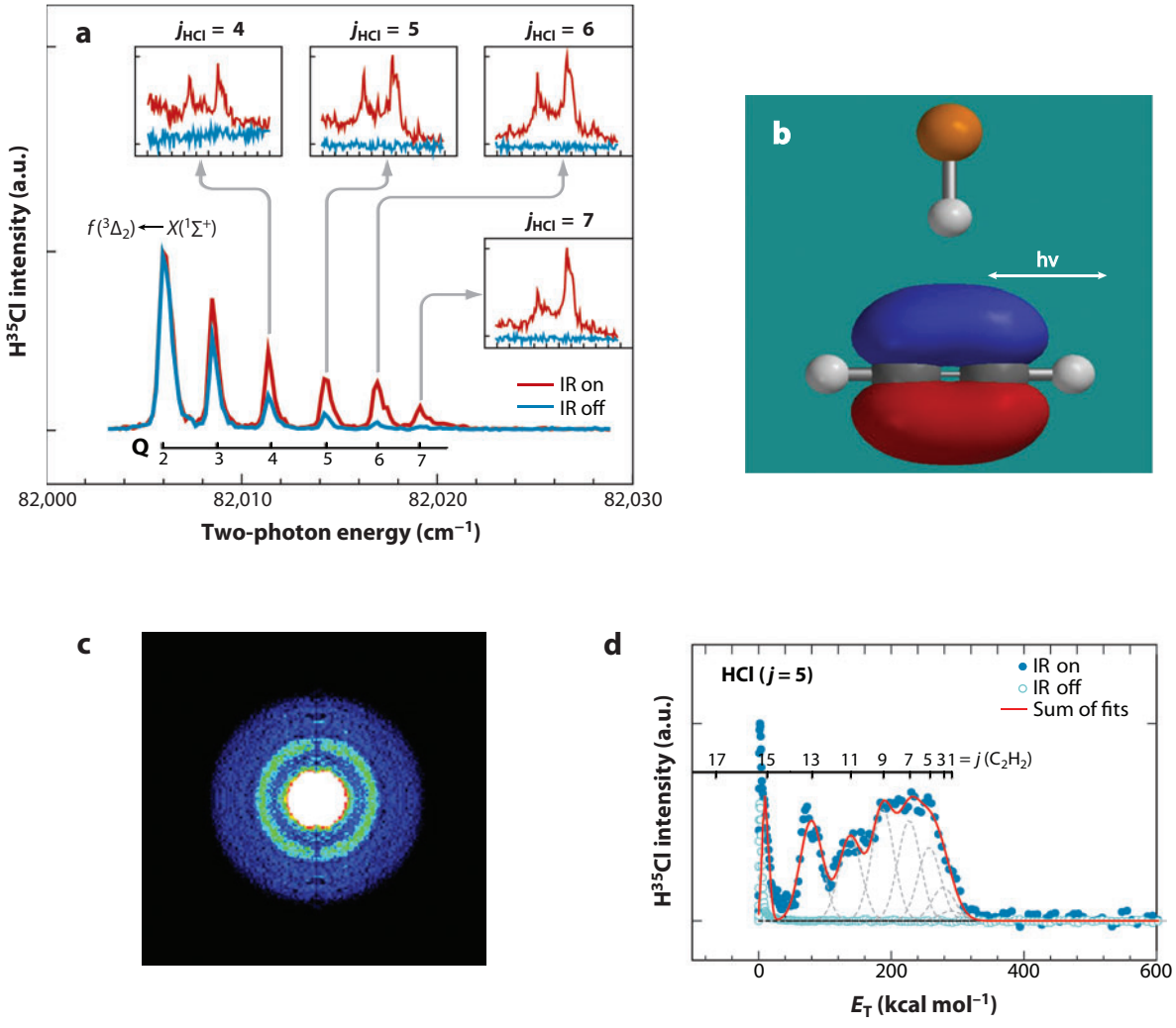

Figure 5

Vibrational predissociation of the C_2H_2-HCl dimer. (*a*) The spectrum depicts the 2 + 1 resonant ionization spectrum of the HCl photofragment. The *x* axis displays the energies required to reach the intermediate *f* state of HCl. The spectrum obtained when the infrared (IR) laser is on is shown in red, and the background spectrum of HCl monomers in the molecular beam is in blue. (*Insets*) Photofragment yield spectra obtained by scanning the IR laser at approximately 3278 cm^{-1}, the region of the asym-CH stretch excitation in the dimer, while monitoring specific rotational levels of HCl(*j*). The spectra are identical to the absorption spectrum of the dimer, whose geometry is shown in panel *b*. (*c*) An image and (*d*) the corresponding center-of-mass recoil energy distribution (*blue dots*) obtained by exciting the dimer to the $K = 0$ level of the asym-CH stretch and monitoring HCl products in $j = 5$. The numbered scale above the data shows the corresponding rotational levels of the acetylene cofragment (only odd levels are allowed). The gray dotted lines are basis Gaussian functions used to fit the recoil energy distribution, and the red curve is the sum of fits that best simulates the experimental spectrum. The fit shows that the distribution of energy in the acetylene cofragment is statistical-like (for further details, see 81). Figure adapted from data in Reference 81.

Different energy flow patterns are manifest when pumping the asym-CH stretch (3278 cm^{-1}) or the HCl stretch (2807 cm^{-1}). In the former case (72, 81, 82), HCl rotates fast, whereas acetylene retains one quantum of C=C stretch, similar to dissociation of its dimers with HF and OH (70–75). The remaining energy is distributed nearly statistically among acetylene rotational levels and

relative translation. In this case, energy flow within acetylene determines vibrational excitation, and H-atom motion determines rotational excitation. The DCl complex behaves similarly (82), but even though enough energy is available to populate DCl in $v = 1$, such excitation is not found.

Excitation of the dimer's HCl stretch vibration reveals a different energy flow pattern (81). VP populates only excited bending vibrational levels in acetylene, and the distribution of translational energy is largely independent of HCl(j). This suggests a constraint in converting linear to angular momentum (78, 79, 82).

Calculations using the AM method accurately reproduce the fragment pair-correlated rotational distributions following dissociation of the C_2H_2-HCl dimer initiated by excitation of either the asym-CH stretch or the HCl stretch, and those from C_2H_2-DCl initiated via asym-CH stretch excitation (82). The calculations, which use hard-shaped 3D ellipsoid potentials (78, 79, 85–87), demonstrate that the dimer is bent at the moment of dissociation, and several geometries lead to hydrogen-bond breakage via a clearly identified set of fragment quantum states. The results suggest a hierarchy in the disposal of excess energy and AM among fragment vibration, rotation, and recoil. Deposition of the largest portion of energy into a C_2H_2 vibrational state sets an upper limit on energy and AM remaining for C_2H_2 rotation and fragment recoil for each HCl(j) fragment. The extent of rotational excitation is constrained by the hard-shape potential, dimer geometry, and AM conservation.

4.2. Predissociation of the Linear Acetylene-Ammonia Dimer

We also examined the VP of the acetylene-ammonia dimer, in which acetylene acts as a Lewis acid whose hydrogen is bonded to the nitrogen of ammonia—a strong Lewis base. The dimer has a linear geometry typical of the traditional hydrogen bond (65, 88–91). The intermolecular bond, however, is expected to be fairly weak owing to the low acidity of acetylene, and the dissociation threshold is 900 cm^{-1}, in good agreement with theory (90, 91). The CH-stretch spectrum has a well-resolved rotational structure, indicating a long lifetime (>0.1 ns) (65).

Following asym-CH stretch excitation at 3213.6 cm^{-1} (redshifted by ~75 cm^{-1} from the monomer), we obtained images of fragment $NH_3(v,j)$ states and derived pair-correlated state distributions of the acetylene fragment (92). The most intriguing finding is that both dissociation fragments are generated with vibrational excitation distributed in specific ways. NH_3 is always vibrationally excited with one or two quanta in the umbrella (symmetric bending) mode, ν_2, whereas bending levels (ν_4 and ν_5) that minimize translational energy release are excited in C_2H_2. Although energy disposal follows the general guidelines proposed by Ewing (77), predissociation is state specific with regard to vibrational energy disposal. The main predissociation channel is $NH_3(1\nu_2) + C_2H_2(2\nu_4$ or $1\nu_4 + 1\nu_5)$, and a minor channel, $NH_3(2\nu_2) + C_2H_2(1\nu_4)$, is also observed (i.e., only channels with energy transfer across the hydrogen bond). Other combinations of fragment states that provide pathways with low translational energy release are not populated: (*a*) ground-state ammonia and acetylene with one quantum of the CC stretch, (*b*) ground-state ammonia and acetylene with three quanta of bend, and (*c*) ground-state acetylene and ammonia with one quantum of the asymmetric bend. In all cases, rotational excitation is low, and the AM model shows that dissociation takes place from slightly bent geometries. The picture that emerges is that energy transfer from the high-frequency CH stretch to the intermolecular modes is inefficient and can take place only from specific orientations and impact parameters spanned by motions in the dimer. This restricts energy flow and results in state-specific vibrational distributions in the fragments.

SUMMARY POINTS

1. Predissociation dynamics of weakly bound molecules can be studied in unprecedented detail with an array of photofragment and photoelectron spectroscopies, including VMI, femtosecond TR methods, and TR coincidence measurements.
2. Predissociation pathways of the NO dimer and acetylene dimers with HCl and ammonia reveal state-specific energy flow patterns, coupling among excited electronic states, and exit-channel dynamics, which are encoded in photofragment and photoelectron spectra and images.
3. *cis*-ONNO shows distinct signatures of covalent bonding in its electronic spectroscopy and the evolution of its dissociative electronic states. Particularly noteworthy is the existence of bright CT states (identified by electronic structure calculations) that are coupled to other Rydberg and valence states. Such coupled states might be characteristic of other weakly covalently bound dimers.
4. Product-state distributions in *cis*-ONNO are nonstatistical and characteristic of both restricted IVR and exit-channel dynamics. Time-resolved photoionization measurements exhibit complex evolution from dephasing of the diabatic bound bright state via other electronic states to products.
5. Predissociation of hydrogen-bonded dimers is another area in which recent progress in experiment and theory has been achieved. Pair-correlated studies using VMI reveal state-specific patterns in vibrational energy flow, reflecting the need to generate simultaneously fragments' vibrational and rotational excitation from a restricted range of impact parameters. In the absence of detailed potential energy surfaces, rotational distributions in the predissociation of C_2H_2-HCl(DCl) and C_2H_2-NH_3 have been simulated successfully using the AM model, and efforts in making this model more predictive are under way (A.J. McCaffery, private communication). Recent results on the predissociation of the H_2O-NH_3 dimer reinforce the conclusions described above (A. Mollner, B. Caterline & H. Reisler, unpublished data).

FUTURE ISSUES

1. Weakly covalently bound dimers are important in the upper atmosphere and on cold surfaces, as well as in other environments in which weak bonds are stabilized. Better understanding of the structure and dynamics of small dimers (such as those of NO_2, ClO, and BrO) can now be achieved with a combination of state-of-the-art techniques and high-level theory. Especially promising is the ability of TRCIS to observe, in favorable cases, dissociation and ionization in the molecular frame, revealing details that are masked in laboratory-frame measurements.
2. By using spectroscopy in helium droplets, it is now possible to assign unambiguously spectral signatures not only of dimers but also of trimers and larger clusters, and predissociation measurements can be carried out, for example, on the water and ammonia cyclic trimers. Hydrogen-bonded aggregates are important in mixed ices in the solar system, and spectroscopy and dynamical studies on prototypical small cluster systems are needed to better understand the ice's stability and properties.

3. The contributions of theoretical modeling are crucial to the understanding of complex systems. Electronic structure and dynamical calculations can identify surface couplings and propagation through conical intersections that lead eventually to products. Simplified but predictive models for product vibrational and rotational distributions in inefficient (slow) VP processes of weakly bound species would be useful in identifying propensity rules for systems that are beyond the reach of present high-level calculations.

DISCLOSURE STATEMENT

The author is not aware of any biases that might be perceived as affecting the objectivity of this review.

ACKNOWLEDGMENTS

It is a pleasure to acknowledge the members of my group, past and present, who have participated in the work described in this review: Andrey Demyanenko, Aaron Potter, Vladimir Dribinski, Igor Fedorov, Guosheng Li, Jessica Parr, Andrew Mollner, and Blithe Casterline. I have benefited greatly from in-depth discussions with and the wisdom of my collaborators: Anthony J. McCaffery, Albert Stolow, Allan East, Oliver Geßner, Sergey Levchenko, and Anna Krylov. Research support from the National Science Foundation, the U.S. Department of Energy, and the Air Force Office of Scientific Research is gratefully acknowledged.

LITERATURE CITED

1. **Whittaker BJ, ed. 2003. *Imaging in Molecular Dynamics: Technology and Applications*. New York: Cambridge Univ. Press**
2. **Suits AG, Continetti RE, eds. 2001. *Imaging in Chemical Dynamics*. Washington, DC: Am. Chem. Soc.**
3. Stolow A, Bragg AE, Neumark DM. 2004. Femtosecond time-resolved photoelectron spectroscopy. *Chem. Rev.* 104:1719–57
4. Stolow A. 2003. Femtosecond time-resolved photoelectron spectroscopy of polyatomic molecules. *Annu. Rev. Phys. Chem.* 54:89–119
5. Heck AJR, Chandler DW. 1995. Imaging techniques for the study of chemical reaction dynamics. *Annu. Rev. Phys. Chem.* 46:335–72
6. Parker DH, Eppink A. 1997. Velocity map imaging of ions and electrons using electrostatic lenses: applications in photoelectron and photofragment ion imaging of molecular oxygen. *Rev. Sci. Instrum.* 68:3477–84
7. **Ashfold MNR, Nahler NH, Orr-Ewing AJ, Vieuxmaire OPJ, Toomes RL, et al. 2006. Imaging the dynamics of gas phase reactions. *Phys. Chem. Chem. Phys.* 8:26–53**
8. Offerhaus H, Nicole C, Lepine F, Bordas C, Rosca-Pruna F, Vrakking M. 2001. A magnifying lens for velocity map imaging of electrons and ions. *Rev. Sci. Instrum.* 72:3245–48
9. Wrede E, Laubach S, Schulenburg S, Brown A, Wouters E, et al. 2001. Continuum state spectroscopy: a high resolution ion imaging study of IBr photolysis in the wavelength range 440–685 nm. *J. Chem. Phys.* 114:2629–46
10. Dribinski V, Ossadtchi A, Mandelshtam VA, Reisler H. 2002. Reconstruction of Abel-transformable images: the basis-set expansion Abel transform method. *Rev. Sci. Instrum.* 73:2634–42
11. Davies JA, LeClaire JE, Continetti RE, Hayden CC. 1999. Femtosecond time-resolved photoelectron-photoion coincidence imaging studies of dissociation dynamics. *J. Chem. Phys.* 111:1–4

1. Comprehensive monograph of all aspects of photofragment and photoelectron imaging.

2. Compilation of articles that includes time-resolved photoelectron imaging and orientation and alignment effects.

7. Recent comprehensive review that includes newer techniques such as slice imaging and applications to bimolecular reactions.

12. Davies JA, Continetti RE, Chandler DW, Hayden CC. 2000. Femtosecond time-resolved photoelectron angular distributions probed during photodissociation of NO_2. *Phys. Rev. Lett.* 84:5983–86
13. Kukolich SG. 1983. Structure and quadrupole coupling measurements on the NO dimer. *J. Mol. Spectrosc.* 98:80–86
14. Western CM, Langridge-Smith PRR, Howard BJ, Novick SE. 1981. Molecular-beam electric resonance spectroscopy of the nitric-oxide dimer. *Mol. Phys.* 44:145–60
15. Hetzler JR, Casassa MP, King DS. 1991. Product energy correlations in the dissociation of overtone excited NO dimer. *J. Phys. Chem.* 95:8086–95
16. Potter AB, Dribinski V, Demyanenko AV, Reisler H. 2003. Exit channel dynamics in the UV photodissociation of the NO dimer to NO(A) and NO(X). *J. Chem. Phys.* 119:7197–205
17. Wade EA, Cline JI, Lorenz KT, Hayden C, Chandler DW. 2002. Direct measurement of the binding energy of the NO dimer. *J. Chem. Phys.* 116:4755–57
18. Mason J. 1975. The dimeric nitrogen oxides. Part 1. Electronic absorption of the nitrogen oxide dimer, and comparison of observed and calculated spectra for dinitrogen dioxide, trioxide and tetraoxide. *J. Chem. Soc. Dalton Trans.* 1975:19–22
19. East ALL. 1998. The 16 valence electronic states of nitric oxide dimer $(NO)_2$. *J. Chem. Phys.* 109:2185–93
20. Sayós R, Valero R, Anglada JM, Gonzalez M. 2000. Theoretical investigation of the eight low-lying electronic states of the cis- and trans-nitric oxide dimers and its isomerization using multiconfigurational second-order perturbation theory (CASPT2). *J. Chem. Phys.* 112:6608–24
21. Tobita M, Perera SA, Musial M, Bartlett RJ, Nooijen M, Lee JS. 2003. Critical comparison of single-reference and multireference coupled-cluster methods: geometry, harmonic frequencies, and excitation energies of N_2O_2. *J. Chem. Phys.* 119:10713–23
22. Levchenko SV, Reisler H, Krylov AI, Geßner O, Stolow A, et al. 2006. Photodissociation dynamics of the NO dimer. I. Theoretical overview of the UV singlet excited states. *J. Chem. Phys.* 125:84301–13
23. Li YM, Vo CK. 2006. Multireference configuration interaction studies on the ground and excited states of N_2O_2: the potential energy curves of N_2O_2 along N-N distance. *J. Chem. Phys.* 125:94303–9
24. Taguchi N, Mochizuki Y, Ishikawa T, Tanaka K. 2008. Multi-reference calculations of nitric oxide dimer. *Chem. Phys. Lett.* 451:31–36
25. Billingsley J, Callear AB. 1971. Investigation of the 2050 Å system of the nitric oxide dimer. *Trans. Faraday Soc.* 67:589–97
26. Forte E, Van Den Bergh H. 1978. The heat of formation of the nitric oxide dimer and its UV spectrum. *Chem. Phys.* 30:325–31
27. Naitoh Y, Fujimura Y, Honma K, Kajimoto O. 1995. Vector correlations in the 193 nm photodissociation of the NO dimer. *J. Phys. Chem.* 99:13652–58
28. Naitoh Y, Fujimura Y, Kajimoto O, Honma K. 1992. Photodissociation of the NO dimer: rotational energy distribution and alignment of $NO(B^2\Pi)$ fragment. *Chem. Phys. Lett.* 190:135–40
29. Naitoh Y, Fujimura Y, Honma K, Kajimoto O. 1993. Photodissociation of the NO dimer at 193 nm: the rotational alignment of the NO(A) fragments. *Chem. Phys. Lett.* 205:423–28
30. Dribinski V, Potter AB, Fedorov I, Reisler H. 2004. Photoexcitation of the NO dimer below the threshold of the NO(A) + NO(X) channel: a photoion and photoelectron imaging study. *Chem. Phys. Lett.* 385:233–38
31. Demyanenko AV, Potter AB, Dribinski V, Reisler H. 2002. NO angular distributions in the photodissociation of $(NO)_2$ at 213 nm: deviations from axial recoil. *J. Chem. Phys.* 117:2568–77
32. Casassa MP, Woodward AM, Stephenson JC, King DS. 1986. Picosecond measurements of the dissociation rates of the nitric-oxide dimer $v_1 = 1$ and $v_5 = 1$ levels. *J. Chem. Phys.* 85:6235–37
33. Casassa MP, Stephenson JC, King DS. 1986. Vibrational predissociation of the nitric-oxide dimer: total energy distribution in the fragments. *J. Chem. Phys.* 85:2333–34
34. Casassa MP, Stephenson JC, King DS. 1988. Time-and state-resolved measurements of nitric oxide dimer infrared photodissociation. *J. Chem. Phys.* 89:1966–76
35. Tachibana A, Suzuki T, Yamato M, Yamabe T. 1990. A theoretical study of the vibrational predissociation of $(NO)_2$. *Chem. Phys.* 146:245–56

36. Matsumoto Y, Ohshima Y, Takami M. 1990. Mode-specific infrared photodissociation of nitric-oxide dimers: high-resolution infrared spectroscopy of $(^{14}NO)_2$ and $(^{15}NO)_2$. *J. Chem. Phys.* 92:937–42
37. Potter AB, Wei J, Reisler H. 2005. Photoinitiated predissociation of the NO dimer in the region of the second and third NO stretch overtones. *J. Phys. Chem. B* 109:8407–14
38. Blanchet V, Stolow A. 1998. Nonadiabatic dynamics in polyatomic systems studied by femtosecond time-resolved photoelectron spectroscopy. *J. Chem. Phys.* 108:4371–74
39. Tsubouchi M, Suzuki T. 2003. Excitation energy dependence in the electronic dephasing time of the NO dimer. *Chem. Phys. Lett.* 382:418–25
40. Tsubouchi M, de Lange CA, Suzuki T. 2003. Femtosecond time-resolved charged particle imaging studies of the UV photodissociation of the NO dimer. *J. Chem. Phys.* 119:11728–39
41. Tsubouchi M, de Lange CA, Suzuki T. 2005. Ultrafast dissociation processes in the NO dimer studied with time-resolved photoelectron imaging. *J. Electron Spectrosc. Relat. Phenom.* 142:193–205
42. Geßner O, Lee AMD, Shaffer JP, Reisler H, Levchenko SV, et al. 2006. Femtosecond multidimensional imaging of a molecular dissociation. *Science* 311:219–22
43. Urban B, Strobel A, Bondybey V. 1999. $(NO)_2$ dimer and its ions: Is the solution near? *J. Chem. Phys.* 111:8939–49
44. Dribinski V, Potter AB, Fedorov I, Reisler H. 2004. Two-photon dissociation of the NO dimer in the region 7.1–8.2 eV: excited states and photodissociation pathways. *J. Chem. Phys.* 121:12353–60
45. Demyanenko AV, Dribinski V, Reisler H, Meyer H, Qian C. 1999. Product quantum-state-dependent anisotropies in photoinitiated unimolecular decomposition. *J. Chem. Phys.* 111:7383–96
46. Mordaunt DH, Ashfold MNR, Dixon RN. 1996. Photodissociation dynamics of A state ammonia molecules. I. State dependent μ–v correlations in the $NH_2(ND_2)$ products. *J. Chem. Phys.* 104:6472–81
47. North SW, Hall GE. 1996. Quantum phase space theory for the calculation of $v \cdot j$ vector correlations. *J. Chem. Phys.* 104:1864–74
48. Domcke W, Yarkony DR, Köppel H, eds. 2004. *Conical Intersections: Electronic Structure, Dynamics and Spectroscopy*. Adv. Ser. Phys. Chem. 15. River Edge, NJ: World Sci.
49. Latimer WM, Rodebush WH. 1920. Polarity and ionization from the standpoint of the Lewis theory of valence. *J. Am. Chem. Soc.* 42:1419–33
50. Bernal JD, Fowler RH. 1933. The theory of water and ionic solutions with particular reference to hydrogen and hydroxyl ions. *J. Chem. Phys.* 1:515–48
51. Bernal JD. 1964. The structure of liquids. *Proc. R. Soc. Lond. Ser. A* 280:299–322
52. Pauling L. 1928. The shared-electron chemical bond. *Proc. Natl. Acad. Sci. USA* 14:359–62
53. Pauling L, ed. 1939. *The Nature of the Chemical Bond and the Structure of Molecules and Crystals: An Introduction to Modern Structural Chemistry*. New York: Cornell Univ. Press
54. Scheiner S, ed. 1997. *Hydrogen Bonding: A Theoretical Perspective*. New York: Oxford Univ. Press
55. Steiner T. 2002. The hydrogen bond in the solid state. *Angew. Chem. Int. Ed. Engl.* 41:48–76
56. Zwier TS. 1996. The spectroscopy of solvation in hydrogen-bonded aromatic clusters. *Annu. Rev. Phys. Chem.* 47:205–41
57. Rohrbacher A, Halberstadt N, Janda KC. 2000. The dynamics of noble gas-halogen molecules and clusters. *Annu. Rev. Phys. Chem.* 51:405–33
58. Oudejans L, Miller RE. 2001. Photofragment translational spectroscopy of weakly bound complexes: probing the interfragment correlated final state distributions. *Annu. Rev. Phys. Chem.* 52:607–37
59. Hutson JM. 1990. Intermolecular forces from the spectroscopy of van der Waals molecules. *Annu. Rev. Phys. Chem.* 41:123–54
60. Heaven MC. 1992. Spectroscopy and dynamics of open-shell van der Waals molecules. *Annu. Rev. Phys. Chem.* 43:283–310
61. Loomis RA, Lester MI. 1997. OH-H_2 entrance channel complexes. *Annu. Rev. Phys. Chem.* 48:643–73
62. Pimentel GC, McClellan AL. 1971. Hydrogen bonding. *Annu. Rev. Phys. Chem.* 22:347–85

41. Review that includes many references on the NO dimer.

58. Comprehensive review on VP of dimers with many references to previous work.

63. Scheiner S. 1994. Ab initio studies of hydrogen bonds: the water dimer paradigm. *Annu. Rev. Phys. Chem.* 45:23–56
64. Nesbitt DJ. 1994. High-resolution, direct infrared laser absorption spectroscopy in slit supersonic jets: intermolecular forces and unimolecular vibrational dynamics in clusters. *Annu. Rev. Phys. Chem.* 45:367–99
65. Hilpert G, Fraser GT, Pine AS. 1996. Vibrational couplings and energy flow in complexes of NH_3, HCN and HCCCCH. *J. Chem. Phys.* 105:6183–91
66. Miller RE. 1989. Vibrationally induced dynamics in hydrogen bonded complexes. *Acc. Chem. Res.* 23:10–16
67. Huang ZS, Miller RE. 1987. Infrared spectroscopy and vibrational predissociation of C_2H_2-HF. *J. Chem. Phys.* 86:6059–64
68. Huang ZS, Miller RE. 1989. Mode-specific vibrational relaxation in the acetylene-hydrogen fluoride binary complex. *J. Chem. Phys.* 90:1478–83
69. Moore DT, Oudejans L, Miller RE. 1999. Pendular state spectroscopy of an asymmetric top: parallel and perpendicular bands of acetylene-HF. *J. Chem. Phys.* 110:197–208
70. Oudejans L, Moore DT, Miller RE. 1999. State-to-state vibrational predissociation dynamics of the acetylene-HF-complex. *J. Chem. Phys.* 110:209–19; Erratum. 110:7109
71. Dayton DC, Block PA, Miller RE. 1991. Spectroscopic evidence for near-resonant intermolecular energy transfer in the vibrational predissociation of C_2H_2-HX, C_2H_2-DX (X = C1, Br and I) complexes. *J. Phys. Chem.* 95:2881–88
72. Oudejans L, Miller RE. 1999. State-to-state vibrational predissociation dynamics of the acetylene-HCl complex. *J. Phys. Chem.* 103:4791–97
73. Davey JB, Greenslade ME, Marshall MD, Lester MI, Wheeler MD. 2004. Infrared spectrum and stability of a π-type hydrogen-bonded complex between the OH and C_2H_2 reactants. *J. Chem. Phys.* 121:3009–18
74. Marshall MD, Lester MI, Wheeler MD. 2004. Spectroscopic implications of the coupling of unquenched angular momentum to rotation in OH-containing complexes. *J. Chem. Phys.* 121:3019–29
75. Marshall MD, Davey JB, Greenslade ME, Lester MI. 2004. Evidence for partial quenching of orbital angular momentum upon complex formation in the infrared spectrum of OH-acetylene. *J. Chem. Phys.* 121:5845–51
76. Ewing GE. 1980. Vibrational predissociation in hydrogen bonded complexes. *J. Chem. Phys.* 72:2096–107
77. Ewing GE. 1987. Selection rules for vibrational energy transfer: vibrational predissociation of van der Waals molecules. *J. Phys. Chem.* 91:4662–71
78. McCaffery AJ. 2004. A new approach to molecular collision dynamics. *Phys. Chem. Chem. Phys.* 6:1637–57
79. McCaffery AJ, Marsh RJ. 2002. Vibrational predissociation of van der Waals molecules: an internal collision, angular momentum model. *J. Chem. Phys.* 117:9275–85
80. Sampson RK, Bellm SM, McCaffery AJ, Lawrance WD. 2005. Rotational distributions following van der Waals molecule dissociation: comparison between experiment and theory for benzene-Ar. *J. Chem. Phys.* 122:74311–20
81. Li G, Parr JA, Fedorov I, Reisler H. 2006. Imaging study of vibrational predissociation of the HCl-acetylene dimer: pair-correlated distributions. *Phys. Chem. Chem. Phys.* 8:2915–24
82. Pritchard M, Parr JA, Li G, Reisler H, McCaffery AJ. 2007. The mechanism of H-bond rupture: the vibrational predissociation of C_2H_2-HCl and C_2H_2-DCl. *Phys. Chem. Chem. Phys.* 9:6241–52
83. Carcabal P, Broquier M, Chevalier M, Picard-Bersellini A, Brenner V, Millie P. 2000. Infrared spectra of the C_2H_2-HCl complexes: an experimental and ab initio study. *J. Chem. Phys.* 113:4876–84
84. Carcabal P, Brenner V, Halberstadt N, Millie P. 2001. Ab initio anharmonic intermolecular potential of the C_2H_2-HCl hydrogen bonded complex. *Chem. Phys. Lett.* 336:335–42
85. Kreutz TG, Flynn GW. 1990. Analysis of translational, rotational, and vibrational energy transfer in collisions between CO_2 and hot hydrogen atoms: the three-dimensional "breathing" ellipsoid model. *J. Chem. Phys.* 93:452–65
86. Bosanac S. 1980. Two-dimensional model of rotationally inelastic collisions. *Phys. Rev. A* 22:2617–22
87. Bosanac S, Buck U. 1981. Rotational rainbow scattering from an off-center rigid shell model. *Chem. Phys. Lett.* 81:315–19

77. Seminal article about VP of weakly bound species that describes propensity rules that predict predissociation rates.

78. Review article that includes methodology and a variety of applications of the angular momentum model.

82. Includes a discussion with many references on theoretical models of VP of van der Waals complexes.

85. Includes a clear explanation of the 3D ellipsoid model.

88. Fraser GT, Nelson DDN Jr, Charo A, Klemperer W. 1985. Microwave and infrared characterization of several weakly bound NH_3 complexes. *J. Chem. Phys.* 82:2535–46
89. Liu Y, Suhm MA, Botschwina P. 2004. Supersonic jet FTIR and quantum chemical investigations of ammonia/acetylene clusters. *Phys. Chem. Chem. Phys.* 6:4642–51
90. Hartmann M, Radom L. 2000. The acetylene-ammonia dimer as a prototypical C-H. . .N hydrogen-bonded system: an assessment of theoretical procedures. *J. Phys. Chem. A* 104:968–73
91. Spoliti M, Bencivenni L, Ramondo F. 1994. An ab initio HF-SCF and MP2 study of hydrogen bonding and van der Waals interactions: low frequency vibrations of bimolecular complexes. *J. Mol. Struc. (Theochem)* 303:185–203
92. Parr JA, Li G, Fedorov I, McCaffery AJ, Reisler H. 2007. Imaging the state-specific vibrational predissociation of the C_2H_2-NH_3 hydrogen-bonded dimer. *J. Phys. Chem. A* 111:7589–98

Annual Review of
Physical Chemistry

Volume 60, 2009

Contents

Indexes

Errata

An online log of corrections to *Annual Review of Physical Chemistry* articles may be found at http://physchem.annualreviews.org/errata.shtml